Interface exchange processes in $LaAlO_3/SrTiO_3$ induced by oxygen vacancies

Malte Behrmann and Frank Lechermann
I. Institut für Theoretische Physik, Universität Hamburg, D-20355 Hamburg, Germany

Understanding the role of defects in oxide heterostructures is crucial for future materials control and functionalization. We hence study the impact of oxygen vacancies (OVs) at variable concentrations on orbital- and spin exchange in the $LaAlO_3/SrTiO_3$ interface by first principles many-body theory and real-space model-Hamiltonian techniques. Intricate interplay between Hubbard U and Hund's coupling $J_{\rm H}$ for OV-induced correlated states is demonstrated. Orbital polarization towards an effective e_g state with predominant local antiferromagnetic alignment on Ti sites near OVs is contrasted with $t_{2g}(xy)$ states with ferromagnetic tendencies in the defect-free regions. Different magnetic phases are identified, giving rise to distinct net-moment behavior at low and high OV concentrations. This provides a theoretical basis for prospective tailored magnetism by defect manipulation in oxide interfaces.

PACS numbers: 73.20.-r,71.27.+a, 75.70.Cn

I. INTRODUCTION

There is strong evidence from recent experiments that oxygen vacancies play a crucial role in the physics of heterostructures between $LaAlO_3$ (LAO) and $SrTiO_3$ (STO) [1–5], as well as for surface [6–8] and bulk [9] features of pure STO. For instance, they may be relevant for ferromagnetic (FM) and superconducting order found in LAO/STO [10–14]. OVs serve as electron dopants and can render an otherwise band-insulating environment metallic [12]. The released charge from O^{2-} fills the Ti($3d$) shell, which has d^0 occupancy in stoichiometric STO. This introduces effects of electron correlation in strontium titanate [15–19], a compound adjacent to the Mott-insulating $3d^1$ $R\mathrm{TiO}_3$ series (R: rare-earth ion) with a Ti($3d^1$) configuration. On similar grounds, the vacancy-induced doping enhances correlations in the LAO/STO interface. Puzzling interplay between itinerant and localized electrons in STO-based surfaces and interfaces is indeed suggested from scanning-tunneling spectroscopy [20–22], magnetoresistance and anomalous Hall-effect measurements [23], resonant x-ray scattering [24, 25] and photoemission [6, 7, 26].

A deeper comprehension of the defect influence on the interface phenomenology is motivated not just by basic research [27]. Since the physical properties of oxide heterostructures, ranging from insulating and/or conducting to magnetic and/or superconducting, may be subtly tuned by the presence of impurities, promising engineering aspects emerge. Due to increasing control in detailed oxide-interface fabrication, new opportunities in high-response materials design are within reach [28]. In view of future spintronics devices, selective magnetic activation on the nano scale by versatile ways of defect creation [29] may soon become available.

Theoretical accounts of realistic LAO/STO heterostructures are challenging because of the unique combination of complexity from the basic interacting quantum perspective and the structural bulk-to-interface setting. Calculations based on density functional theory (DFT) using hybrid functionals or employing static correlation effects from a Hartree-Fock-like treated Hubbard Hamiltonian ('+U') can reveal some relevant aspects of the intriguing electronic structure [15–17, 30–34]. But there are two serious drawbacks to such extended Kohn-Sham schemes. Broken-symmetry states, i.e. long-range magnetic and/or charge orders, have to be stabilized often right from the start to address correlation effects. Second, several many-body hallmarks such as paramagnetic local-moment behavior, low-energy quasiparticle (QP) formation, band narrowing, and interplay between QPs and Hubbard bands are not incorporated due to a lack of frequency dependence in the local electronic self-energy Σ. Invoking DFT+dynamical mean-field theory (DMFT) overcomes these deficiencies, but, especially for defect environments treated by larger cells [19, 35], it remains numerically expensive. It is important to note that many-body physics beyond standard DFT-based approaches is here not only a detail, but essential for illuminating mechanisms of future technological use. As a further relevant aspect, first-principles supercell computations to reveal defect influences are generally not perfectly suited to the problem at hand. They are restricted by the choice of the (often too small) cell size and can introduce artifacts because of the introduced short-range defect ordering.

In this theoretical work we want to focus on the peculiar problem of OVs at the LAO/STO interface over a larger concentration range. Though a deeper relevance of these defects for the formation of the original quasi-twodimensional electron liquid is still under debate, several first-principles calculations have shown that even the stoichiometric heterostructure is metallic from partly filled Ti(t_{2g})-dominated bands at the Fermi level. Although there are other theoretical suggestions [32, 36–40], OVs provide a natural way to explain the occurrence of interface ferromagnetism [16, 19, 30, 34]. In conventional DFT, an OV induces crystal-field lowered e_g-like impurity states on the neighboring Ti ions. Thinking intuitively, two limiting scenarios could apply depending on the concentration of vacancies in LAO/STO. Lin and Demkov [18, 41] studied the dilute-defect limit with only

few oxygen defects, where e_g-like local moments on assumed Anderson/Kondo impurities may form. The latter can couple ferromagnetically via Ruderman-Kittel-Kasuya-Yosida (RKKY) interaction mediated by the itinerant t_{2g} electrons. On the other hand, in a dense-defect limit, the physics is closer to a minimal two-orbital (e_g, t_{2g}) Hubbard model near quarter filling [19, 42]. In a recent DFT+DMFT work [19] it was shown that in this limit, emerging FM order in the interface TiO_2 layer can indeed be explained by effective (Zener) double-exchange [43, 44] between an vacancy-induced $\tilde{e_g}$ orbital and an in-plane $t_{2g}(xy)$ orbital. Michaeli *et al.* [36] also proposed Zener exchange between localized and itinerant states, but without referring to OVs as the source for localization.

Although experimentally the influence of OVs in STO-based materials is documented by monitoring physical response with varying oxygen partial pressure [4, 8, 21], a good quantitative understanding of the OV concentration as well as definite information on the location with respect to the interface [2, 4] is still lacking. To cope with the uncertainties in the number of OVs, we here perform investigations in a broad concentration range. In order to achieve this task, the correlated electronic structure is treated in a real-space framework allowing for in principle arbitrary vacancy configurations in number and arrangement. Depending on the concentration of OVs, we encounter different orbital- and spin-exchange regimes, that shed light on the emerging FM order at the LAO/STO interface. Local and non-local processes subject to a subtle interplay between the Hubbard U and Hund's $J_{\rm H}$ govern the OV-induced magnetism. Throughout the paper all energies are given in electron volts.

The paper is organized as follows. To set the stage, we touch base with previous DFT+DMFT calculations [19] and start in Sec. II with a brief view on the impact of the Hund's coupling $J_{\rm H}$ on the magnetic order in a n-type [45] LAO/STO interface in the limit of high OV concentration. In Sec. III A the correlated real-space modeling to describe different defect concentrations is introduced. Results in the dilute limit of a single oxygen vacancy as well as of two OVs in the interface are presented in Sec. III B. Section III C deals with the evolution of electron correlation and magnetism upon increasing the number of OVs from the dilute- to a dense-defect limit. The work closes with a discussion and summary in Sec. IV.

II. INFLUENCE OF $J_{\rm H}$ IN THE DENSE-DEFECT LIMIT OF OXYGEN VACANCIES IN LAO/STO

A charge self-consistent DFT+DMFT study in a dense-defect limit of 25% OVs in the TiO_2 interface layer was performed in Ref. 19. We define that limit by OVs exclusively located in the TiO_2 interface layer, with each Ti ion having one OV in bonding distance (see Fig. 1). Here and throughout this paper Ti neighborhoods with more than one nearby OV are not considered.

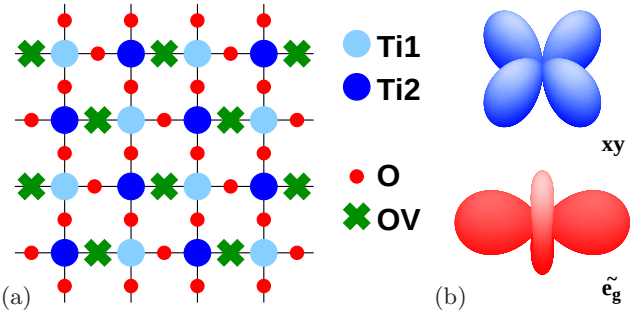

FIG. 1. (color online) (a) TiO_2 interface layer of n-type LAO/STO with 25% oxygen vacancies utilized in supercell DFT+DMFT calculations [19]. Ions Ti1 and Ti2 form the basis in the $\sqrt{2}\times\sqrt{2}$ primitive cell. (b) minimal relevant Ti orbitals with $|\tilde{e_g}\rangle \sim 0.55|z^2\rangle \pm 0.84|x^2-y^2\rangle$ [19].

For the DFT part a mixed-basis pseudopotential framework is used and the DMFT impurity problems are solved by continuous-time quantum Monte Carlo (CT-QMC) [46–49]. A minimal correlated subspace was derived to consist of a two-orbital [$\tilde{e_g}$, $t_{2g}(xy)$] manifold located at the interface Ti ions. Remaining t_{2g} orbital degrees of freedom are included in more distant layers from the interface. The local Coulomb interactions in the interacting Hamiltonian with Slater-Kanamori parametrization, i.e., the Hubbard U and Hund's exchange $J_{\rm H}$ were set to U=2.5 and $J_{\rm H}$=0.5, in line with other works [16]. A double-exchange-like (DE) mechanism is effective in stabilizing FM order within the interface. Thereby the spin polarization is triggered by inter-orbital scattering between the nearly-localized $\tilde{e_g}$ state and the less-localized xy state. Because of this exchange mechanism, the fewer and more-itinerant xy electrons exhibit stronger spin polarization. The self-consistently adapting Ti occupation results in a quarter filling ($n_{\rm Ti1,Ti2}\sim$1) of the two-orbital correlated subspace within the interface layer. In total, each OV releases 2 electrons, which add to the 0.5 electrons per Ti ion due to the polar-catastrophe avoidance within LAO/STO heterostructures. In the supercell treatment of the dense-defect limit, which notably includes several TiO_2 layers, these two contributions adjust such that 1 electron per Ti settles in the interface TiO_2 layer. Hence the latter layer formally consists of $Ti^{3+}(3d^1)$ ions in the given defect limit.

Since the size of the Hund's coupling is key to a double-exchange-like mechanism for the onset of ferromagnetism, we here present results from varying $J_{\rm H}$, while keeping U=2.5 fixed. For more details on the calculational setup see Ref. 19. Usually the value of $J_{\rm H}$ is much less modified by screening processes than the Hubbard U and therefore remains close to the magnitude in the free atom. Hence although for LAO/STO a Hund's coupling $J_{\rm H}$=0.5−0.6 is expected, we take the liberty of changing this value in order to assess it relevance for the underlying physics. Figure 2(a) displays the

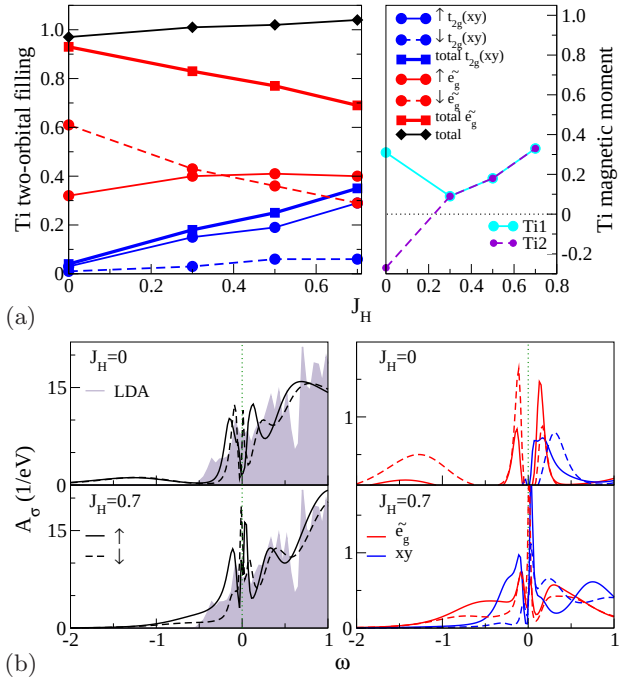

FIG. 2. (color online) DFT-DMFT results depending on $J_{\rm H}$ for the dense-defect LAO/STO interface with magnetic order (T=180K). (a) Orbital occupations (left) and Ti magnetic moment (right). (b) Total (left) and local (right) spectral functions.

orbital- and spin-dependent occupations with $J_{\rm H}$ in the magnetically ordered phase of the dense-defect limit. For $J_{\rm H}\gtrsim$0.4 ferromagnetism with local Ti moment $m\sim$0.2-0.4$\mu_{\rm B}$ occurs. But when $J_{\rm H}$ becomes smaller and eventually tends to zero, antiferromagnetic (AFM) order between the nearest-neighbor (NN) titanium ions sets in. In the latter regime the orbital polarization in favor of the more localized $\tilde{e_g}$ level strongly increases towards nearly full polarization at $J_{\rm H}$=0.

Figure 2(b) shows the k-integrated spectral function $A_\sigma(\omega)=\sum_{\mathbf{k}} A_\sigma(\mathbf{k},\omega)$ in the limiting cases $J_{\rm H}$=0, 0.7 for the whole supercell as well as for the correlated subspace of the Ti[$\tilde{e_g}$, $t_{2g}(xy)$] states. Concerning the correlation strength the Hund's coupling has a known model impact within a two-orbital system near quarter filling [50]. In the case of vanishing $J_{\rm H}$ stronger correlations occur, giving rise to a prominent lower Hubbard peak at $\sim$−1.3. This incoherent excitation is exclusively associated with the vacancy-induced $\tilde{e_g}$ state and resembles a similar feature in photoemission data [7, 8, 26]. Locally, hopping is nearly blocked on the interface Ti ions and residual metallicity is mainly provided by sites far from the interface. For rather large $J_{\rm H}$ the interface is well conductive, with a prominent QP peak at the Fermi level but an absent lower Hubbard peak. Coexistence of general metallicity with the latter incoherent excitation holds for reasonable intermediate values of $J_{\rm H}$ [19]. The AFM order for $J_{\rm H}$=0 is completely carried by the $\tilde{e_g}$ orbital, while the FM order for $J_{\rm H}$=0.7 is dominantly carried by the xy orbital. These findings underline the importance of DE processes in the formation of ferromagnetism at the LAO/STO interface in the dense-defect limit.

III. REAL-SPACE APPROACH TO OXYGEN VACANCIES IN LAO/STO

The scope is now broadened by addressing lower OV concentrations in the TiO_2 interface layer. Performing large-scale incommensurate studies from first principles of the interplay between defects, disorder and correlations for multi-orbital lattice is nowadays still too expensive. We thus need a minimal setting that is geared to carry the key physics of the OV-doped LAO/STO interface. Therefore a model-Hamiltonian approach is used, inspired by the results of the DFT+DMFT investigation in the previous section.

A. Model and methodology

A two-orbital Hubbard Hamiltonian based on the vacancy-induced effective $\tilde{e_g}$ state and the in-plane $t_{2g}(xy)$ state is employed on a 10×10 square lattice with $N_{\rm Ti}$=100 titanium ions, mimicking the interface TiO_2 layer (see Fig. 3). Only the Ti sublattice is treated explicitly and the oxygen degrees of freedom are integrated out within the chosen Hamiltonian form. Since the creation of OVs amounts to electron doping, explicit involvment of remaining oxygen orbitals can be neglected to first approximation. Periodic boundary conditions are applied. Only intra-orbital NN hoppings are retained in the model.

Lets focus first on the lattice scenario in the dense-defect limit, where each Ti site is affected by a nearby OV, to build up the model characteristics. In line with Ref. 19, we choose $t_{\tilde{e_g}}$=t_{xy}=0.2 for the NN hoppings. In contrast to a different modeling by Pavlenko *et al.* [42], our hopping amplitudes from the projected-local-orbitals method [51] for higher OV concentrations are not strongly orbital dependent. From a noninteracting point of view, the crystal-field splitting Δ between the xy level and the vacancy-induced low-energy $\tilde{e_g}$ is the key model parameter. Note that Δ is different from the usual octahedral crystal-field splitting that is already vital in the stoichiometric compound. The latter energy splitting does not occur in the present defect model. Again from Ref. 19, we set Δ=0.3.

Local electron-electron interactions via the Hubbard U and Hund's coupling $J_{\rm H}$ are applied at all Ti sites. The

full Hamiltonian then reads

$$H = -t \sum_{\langle i,j\rangle\alpha\sigma} c^\dagger_{i\alpha\sigma} c_{j\alpha\sigma} - \sum_{i\sigma} \Delta_i \left(n_{i,\beta,\sigma} - n_{i,xy,\sigma}\right) + \\ + U \sum_{i\alpha} n_{i\alpha\uparrow} n_{i\alpha\downarrow} + \\ + \frac{1}{2} \sum_{i,\alpha\neq\alpha',\sigma} \Big\{ U'\, n_{i\alpha\sigma} n_{i\alpha'\bar{\sigma}} + U''\, n_{i\alpha\sigma} n_{i\alpha'\sigma} + \\ + J_{\rm H} \left(c^\dagger_{i\alpha\sigma} c^\dagger_{i\alpha'\bar{\sigma}} c_{i\alpha\bar{\sigma}} c_{i\alpha'\sigma} + c^\dagger_{i\alpha\sigma} c^\dagger_{i\alpha\bar{\sigma}} c_{i\alpha'\bar{\sigma}} c_{i\alpha'\sigma} \right) \Big\} \ , \qquad (1)$$

where $c(c^\dagger)$ are creation (annihilation) operators, $n{=}c^\dagger c$, i,j are site indices, $\alpha,\alpha'{=}\beta,xy$ and $\sigma{=}\uparrow,\downarrow$ marks the spin projection, using $U'{=}U-2J_{\rm H}$, $U''{=}U-3J_{\rm H}$. For the same Hubbard U, the strength of electronic correlations is usually weaker within slave-boson theory than within CT-QMC. If not otherwise stated the Hubbard U is thus set to $U{=}3$ in all calculations. The Hund's coupling is set to $J_{\rm H}{=}0.55$, again with variations to smaller/larger values to trace its relevance. For the dense-defect limit, $\Delta_i{=}\Delta$ and $\beta{=}\tilde{e_g}$, i.e. the vacancy-induced $\tilde{e_g}$ crystal-field state is active on each Ti site.

In the latter limit every interface Ti ion has one neighboring OV and the given Hamiltonian is coherently applicable on each Ti site. However, when the defect number is reduced, titanium sites without a nearby OV appear and at those Ti sites there are no low-energy $\tilde{e_g}$ states. In the stoichiometric case the e_g orbitals are strongly bound to O($2p$) and do not contribute either to states at the Fermi level or to any possible local-moment formation. In order to keep the modeling simple, we make the following approximations when treating general defect cases in real space: (i) the Hamiltonian of form (1) is used throughout the lattice, (ii) the parametrization of Δ_i is

$$\Delta_i = \begin{cases} \Delta \ , \ \beta = \tilde{e_g} & : \ \text{if an OV nearby} \\ 0 \ \ , \ \beta = xz/yz & : \ \text{if no OV nearby} \end{cases} \qquad (2)$$

and (iii) multiple OVs around a Ti site are prohibited. The interpretation of (ii) is as follows: without a nearby OV, the Ti local low-energy electrons are mainly of t_{2g} kind and thus the former $\tilde{e_g}$ degree of freedom takes over the role of an additional effective t_{2g} orbital. This can be justified by a notable hybridization between $\tilde{e_g}$ and xz, yz in the dense-defect case [19]. We neither change hoppings for Ti sites with or without nearby OVs nor employ a concentration-dependent hopping modification. Such a more detailed parametrization is hard to fix and the aim here is to work in a canonical two-orbital setting.

The final modeling step examines the concentration-dependent electron filling of a lattice with vacancy concentration $c{=}N_{\rm vac}/N_{\rm O}$, where $N_{\rm vac}$ is the number of OVs and $N_{\rm O}{=}2N_{\rm Ti}$ denotes the number of oxygen sites. Our electron count considers only the single TiO_2 interface layer, explicit charge fluctuations to more distant layers across the interface are neglected. In the dense-defect limit of the supercell treatment, DFT+DMFT yields a filling of one electron at each Ti site in the interface TiO_2 layer. Supercell DFT calculations for the defect-free interface result in an itinerant two-dimensional electron system with a count of 0.5 electrons per interface Ti [19], i.e. 50 electrons for the 100 Ti sites, in line with the polar-catastrophe avoidance. Putting these numbers together, we choose the linear-interpolation scheme $n_{\rm tot}{=}N_{\rm Ti}/2{+}N_{\rm vac}$ for the total lattice electron count $n_{\rm tot}$ at intermediate defect levels.

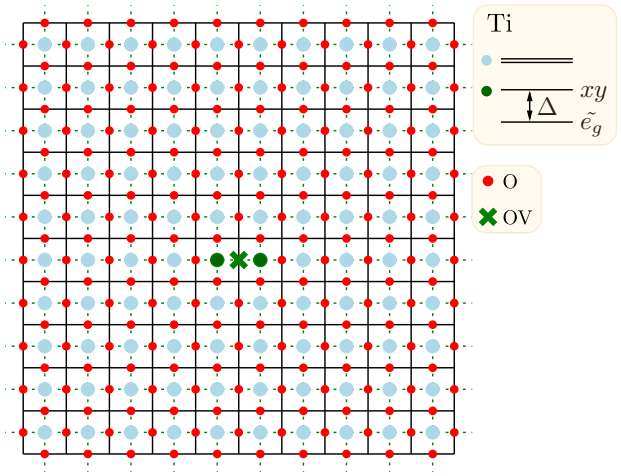

FIG. 3. (color online) Real-space two-orbital modeling on a 10×10 TiO_2 square lattice for the n-type LAO/STO interface.

The interacting multi-orbital problem is solved by a real-space formulation of the rotational-invariant slave-boson (RISB) mean-field method [50, 52–55]. It corresponds to single-site DMFT close to zero temperature with a simpler impurity solver than the CT-QMC, allowing for local self-energies Σ with a linear frequency dependence and static terms. Renormalized QPs as well as local multiplets can be monitored in the interacting regime. Explicit intersite self-energy terms are neglected, but due to the coupling of all sites in the RISB self-consistency cycle effects of incoherency due to the distribution of defects are included. Our real-space approach is reminiscent of a single-orbital variant put into practice by Andrade *et al.* [56]. However instead of simplified Kotliar-Ruckenstein slave bosons [57] we here use the full rotational-invariant extension and elaborate on a multiorbital framework. Because of the model/method complexity no disorder averages are performed in this work. The calculations utilize 60 slave bosons and 17 lagrangian multipliers per site, 7700 variational parameters in total, with dimension 400×400 for the kinetic part of the Hamiltonian.

In the following, the ordered magnetic moment m, the orbital moment τ, the paramagnetic local spin moment

$m_{\rm PM}$ and the orbital polarization ζ are defined as

$$m = \sum_\alpha m_\alpha = \sum_\alpha (\bar{n}_{\alpha\uparrow} - \bar{n}_{\alpha\downarrow}) \ , \ \tau = \sum_\sigma (\bar{n}_{\beta,\sigma} - \bar{n}_{xy,\sigma})$$
$$m_{\rm PM} = \overline{\left(\sum_\alpha S_\alpha\right)^2} \ , \ \zeta = \frac{\sum_\sigma \bar{n}_{\beta,\sigma}}{\sum_\sigma \bar{n}_{xy,\sigma}} \quad , \quad (3)$$

where S denotes the local spin operator and $\bar{\mathcal{O}}=\langle\mathcal{O}\rangle$. Lattice-averaged values $Q_{\rm lat}$ of these quantities Q are computed by $Q_{\rm lat}=Q/N_{\rm Ti}$.

B. Dilute-defect limit

Since our parametrization is adjusted to the DFT+DMFT results within the dense-defect limit, the model performance in the contrary limit of one or two OVs is of primary interest. For the case of two vacancies, a long-distance accommodation is chosen. Furthermore, they are placed on differently directed bars on the effective square lattice to minimize coherency effects.

Figure 4 summarizes the obtained real-space results for key quantities in the PM phase as well as with magnetic order. Each small square resembles one Ti site and the oxygen sites are located in the middle of the enclosing bars. As expected, the orbital polarization towards the $\tilde{e_g}$ level for the Ti sites near vacancies is substantial. Away from the defect, especially in the two-OV case, there are, however, also oscillations in the orbital moment. The local PM spin moment is largest close to the OVs, understood from the well-localized correlated $\tilde{e_g}$ electrons, but attains a minimum just at second-nearest Ti sites.

When initializing the RISB calculations with FM order, at saddle-point the solutions indeed reveal a small net FM lattice moment. But throughout the lattice the site-resolved ordered magnetic moment m alternates. Interestingly, while m for the single-OV case is still rather small at the defect, already the two-OV case displays a strong increase in the absolute value of the near-defect Ti magnetic moment. Furthermore, whereas for the single vacancy the spins on both NN Ti sites align in the same direction, an AFM alignment emerges with two vacancies. This is surprising since the nearby Ti sites in both scenarios show similar strong filling of the localized $\tilde{e_g}$ state. Due to the strongly correlated regime, a significant kinetic exchange $\sim t^2/U$ of AFM type is expected. Therefore the distance between OVs has to matter for the near-defect spin coupling. Structures with defects at closer range favor the local AFM alignment. The nonlocal exchange with the alternating m throughout the lattice may also play a role in the local spin alignment. Thus there appears to be an intricate coupling between short- and longer-range exchange on the lattice.

Note that in general the overall system is rather susceptible to net magnetic order even with only a small number of defects and small resulting moments. The electron count per site reads $\bar{n}$=0.51(0.52) for one(two) OV(s), i.e. in principle the two-orbital Hubbard modeling is close to one-eighth filling. Thus though the stoichiometric interface in DFT+DMFT does not show magnetic order [19], it apparently only needs a low concentration of OVs to create the first magnetic instability in the correlated regime.

In order to investigate the issue of magnetic exchange with distance in more detail, the averaged ordered magnetic moment with spacing r from the OV in the single-defect case is plotted in Fig. 5. The NN Ti site is located in distance $r_{\rm NN}$=0.5 in units of the lattice constant a. Though it is expected that results will dependent on the chosen lattice size, there are significant variations within the shorter- and longer-range regions. For $d\sim$2.5 the moments predominantly change their sign and the spin coupling switches from FM- to AFM-like. Let's assume here a Fermi-wave-vector k_F modulated RKKY exchange with $J(d)\sim\cos(2k_F\,d)$ in the low-density limit for the sea of conduction electrons [36]. This would correspond to $k_F\sim\pi/10$ in reciprocal units, more or less commensurable

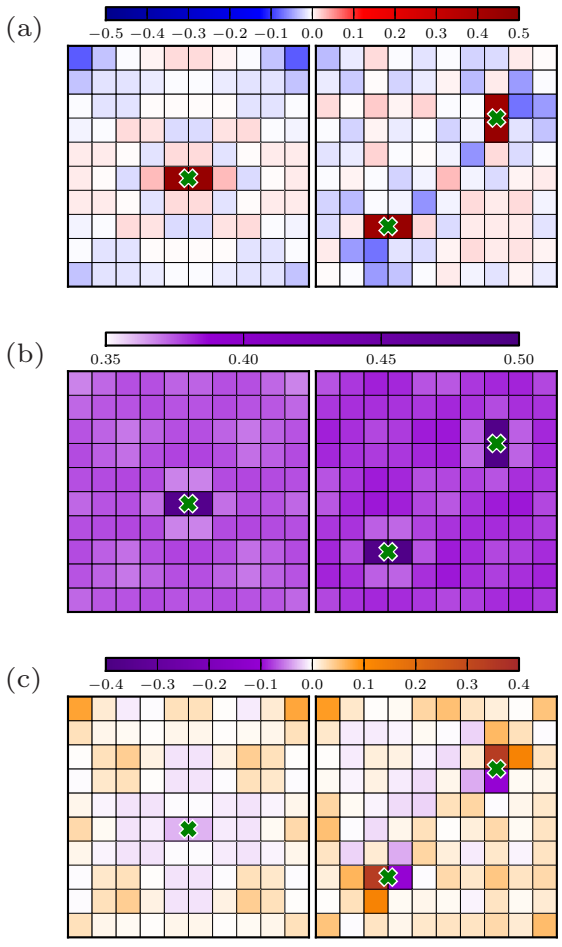

FIG. 4. (color online) Site-resolved quantities of interest for one OV (left) and two OVs (right) in the TiO_2 layer. (a) PM orbital moment τ, (b) PM local spin moment $m_{\rm PM}$, and (c) ordered magnetic moment m.

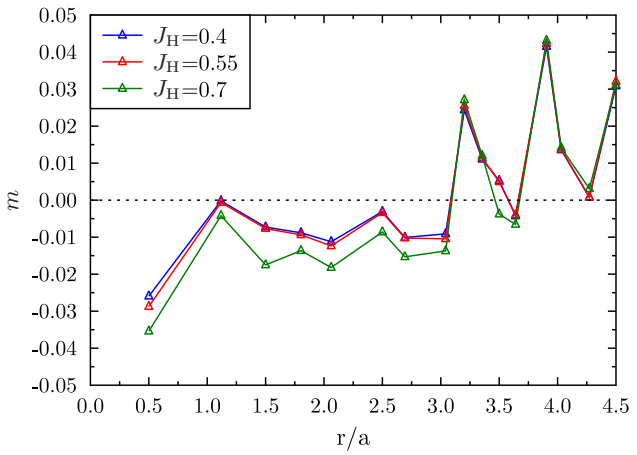

FIG. 5. (color online) Distance-dependent magnetic moment $m(r)$ with the oxygen vacancy at the origin in the magnetically ordered single-defect case for different choices of the Hund's coupling J_H.

with the noted one-eighth filling. But one has to keep in mind that the local ordered moment in our single-OV case is too small for a serious application of the standard RKKY picture. Still, for the record, there are indications of RKKY-like exchange taking place in the dilute-defect limit. Concerning the influence of Hund's coupling, not surprisingly, a larger J_H increases the spin moments since it tends to locally align the contributions from the orbital degrees of freedom.

C. Electron correlation and magnetism from the dilute- to the dense-defect limit

We now investigate the regime between the dilute-defect limit (c=0.005, 0.01) and the dense-defect limit (c=0.25). Additional configurations with randomly distributed OVs for intermediate concentrations are constructed, prohibiting local Ti neighborhoods with more than one vacancy in NN distance, respectively. In the following, site-resolved and site-averaged data is presented. It proves instructive not only to perform full lattice averages, but also to differentiate between the two groups of Ti sites, i.e., those with and those without nearby OVs.

Figure 6 provides a measure of the correlation strength by displaying the paramagnetic QP weight $Z=\left[1-\frac{\partial}{\partial\omega}\Sigma\right]^{-1}_{\omega=0}$. Because of the low electron count at low OV concentrations the lattice QP weight starts off with values close to the noninteracting limit $Z_{\rm lat}$=1. With more vacancies and increased electron doping, general electronic correlations become stronger down to $Z_{\rm lat}\sim$0.4 in the dense-defect case. For the considered electron-doping regimes the Hund's coupling J_H on average weakens correlations, in line with DFT+DMFT results from Sec. II. For any doping, orbital- and/or site-selective Mott transitions remain absent. Not surprisingly, electrons in the $\tilde{e_g}$ orbitals are nonetheless stronger correlated since they are more localized due to the lowered crystal field. While for the xy state an obvious site discrimination occurs only at higher doping, the $\tilde{e_g}$ electrons near OVs are already much heavier at the lowest doping. Interestingly the xy electrons eventually become stronger correlated *away* from near-OV titanium. Thus the vacancy influence on correlations is twofold: it locally strengthens the $\tilde{e_g}$ correlation and nonlocally fosters the xy correlations.

As mentioned, the site-dependent correlation strength is of course related to the local orbital filling, shown in Fig. 7 from low to higher OV-induced electron doping. For comparison, orbital occupations in the noninteracting case (U=J_H=0) are additionally depicted. For the Ti sites with nearby OVs a strong orbital polarization to-

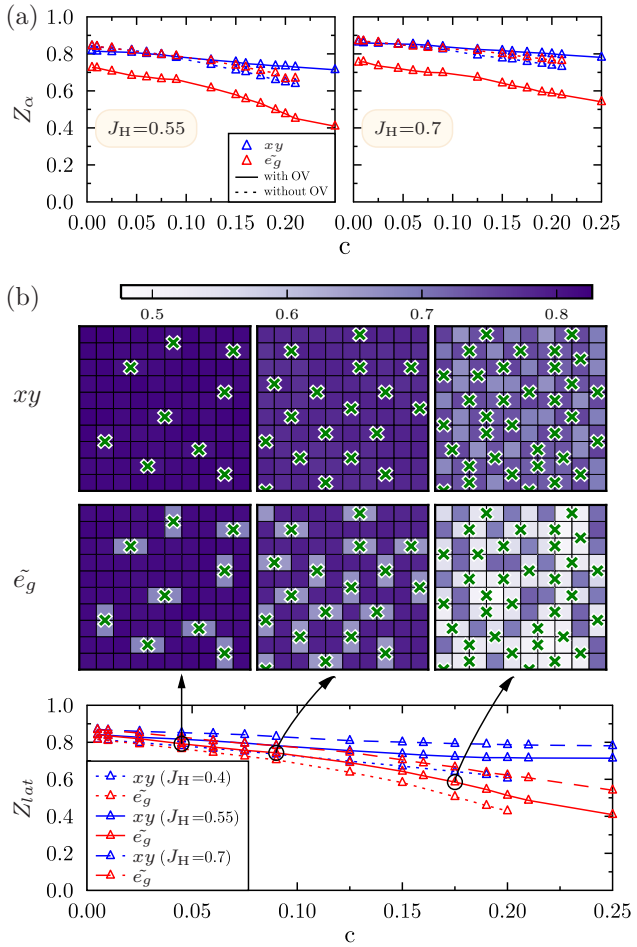

FIG. 6. (color online) Orbital-resolved QP weight Z vs concentration of oxygen vacancies (OVs) in the PM phase. Total electron count increases from $n_{\rm tot}$=51 (1 OV, c=0.005) to $n_{\rm tot}$=100 (50 OVs, c=0.25). (a) Average Z_α for states on Ti sites with and without nearby OVs for J_H=0.55 (left) and J_H=0.7 (right). (b) Site-resolved Z for selected dopings and J_H=0.55 (top) as well as lattice $Z_{\rm lat}$ for different choices of J_H (bottom).

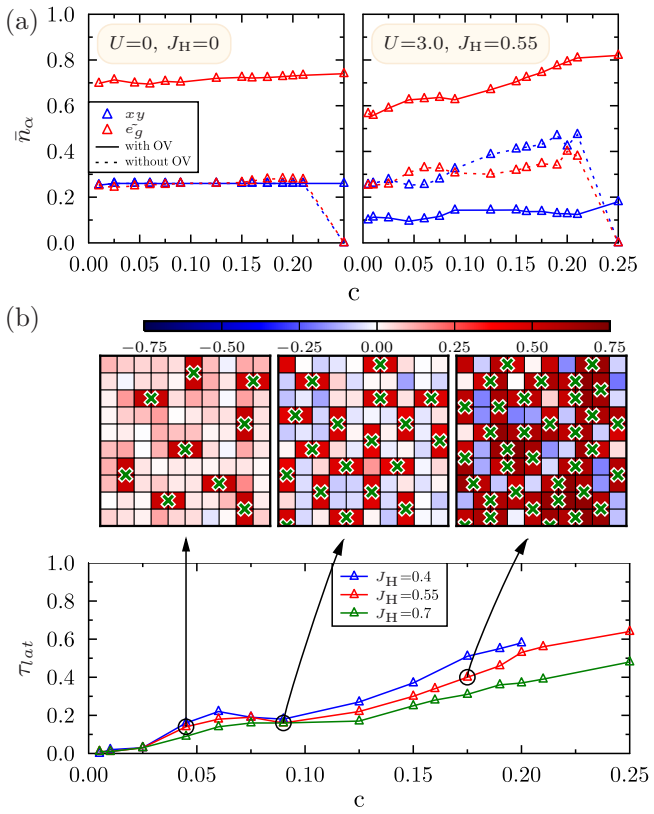

FIG. 7. (color online) Orbital-resolved occupation in the PM phase. (a) Average occupations of Ti sites with and without nearby OVs for the noninteracting (left) and interacting (right) case. (b) Concentration-dependent orbital moment τ in real space (top) and lattice-averaged (bottom).

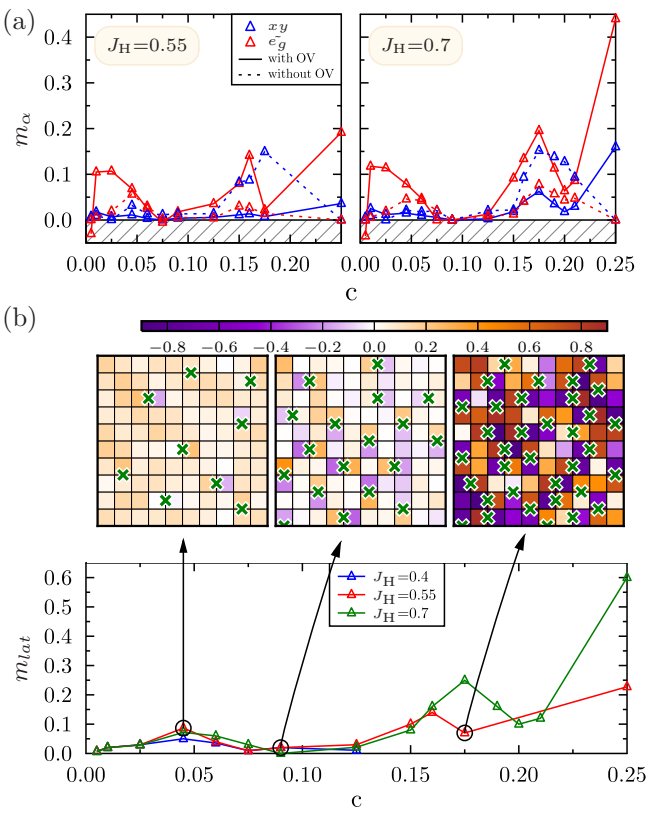

FIG. 8. (color online) Orbital-resolved magnetic moment m. (a) Average magnetic moment of Ti sites with and without nearby OVs for $J_{\rm H}$=0.55 (left) and $J_{\rm H}$=0.7 (right). (b) Concentration-dependent magnetic moment m in real space (top) and lattice-averaged (bottom).

wards $\tilde{e_g}$ already at low dopings is obvious, even without local Coulomb interactions. Rather independent of the number of vacancies, a polarization $\zeta\sim$2.8 holds for these sites in the noninteracting problem. With interactions this orbital polarization is substantially increased for all doping levels because of the crystal-field renormalization via the electronic self-energy. It still gradually decreases from $\zeta\sim$6 in the dilute limit to $\zeta\sim$4 in the dense limit.

Due to the absence of local crystal fields a subtle competition between both orbital degrees of freedom occurs at the remaining Ti sites. However, remember that in this region the '$\tilde{e_g}$' orbital inherits the role of an additional t_{2g} orbital in our modeling. The noninteracting case does not reveal any finite orbital moment for any OV concentration. By including Coulomb interactions, low doping from the dilute limit slightly disfavors the xy orbital. But interestingly, at $c_{\rm p}\sim$0.08 the xy orbital takes over the lead in occupation. Thus also here a nonlocal impact of the OV-induced correlations shows up, breaking the orbital degeneracy at Ti sites away from the defects. Since in the dense-defect limit every Ti ion has one nearby OV, the class of defect-free Ti sites disappears and its nominal filling then, of course, vanishes. Intuitively, the doping-dependent change of orbital-filling hierarchy for this Ti class can be understood as follows. At very low dopings, the interacting system tries to put more electrons into the $\tilde{e_g}$ level, since there they can occasionally enjoy the lower crystal field close to an OV. Yet at some concentration with increased electron filling, it is more beneficial to put electrons which like to visit defect-free regions in the overall less occupied xy levels to minimize the Coulomb interaction and gain kinetic energy.

The real-space variation of the site-dependent orbital moment τ underlines these findings [see Fig. 7(b)]. Beyond the critical doping level $c_{\rm p}$ there is a qualitative change in the polarization of the 'interstitial' region towards xy. A shoulder in the lattice-averaged orbital moment $\tau_{\rm lat}$ is located around $c_{\rm p}$. Of course, every increase in OVs, with strong orbital polarization towards $\tilde{e_g}$ nearby, renders $\tau_{\rm lat}$ further monotonically growing with c. Give or take, the averaged influence of $J_{\rm H}$ on the orbital moment is as expected from multiorbital Hubbard models, i.e. it works against the crystal field and tries to wash out orbital polarization [58].

The orbital- and site-resolved magnetic moment ex-

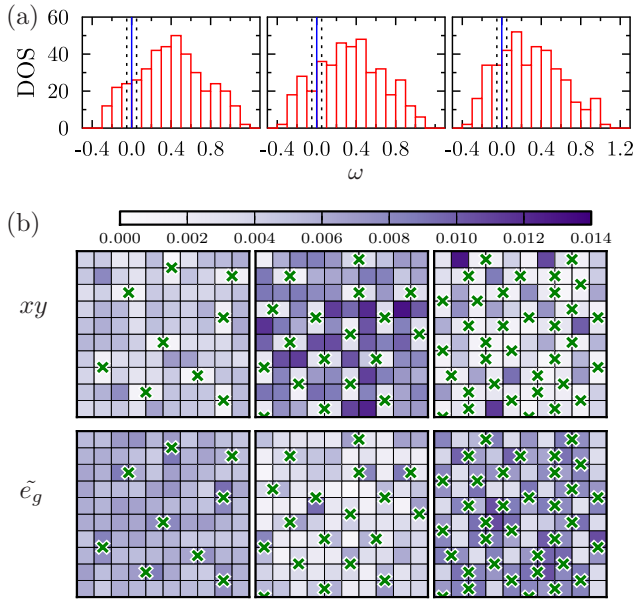

FIG. 9. (color online) Low-energy PM spectral information for dopings c=(0.045, 0.09, 0.175) (left to right) using $J_{\rm H}$=0.55. Orbital-resolved site-contribution $|C_{im}|^2$ to the renormalized QP state $|\Psi_{\rm QP}\rangle$=$\sum_{im} C_{im}|\phi_{im}\rangle$ in an energy window $[-0.05, 0.05]$ around the Fermi level.

hibits an even more intricate structure with respect to the vacancy concentration (cf. Fig. 8). Starting from the dilute-defect limit the Ti sites with nearby OVs can be divided into two subclasses. One spin thereof compensates their net moment by AFM alignment, the other one displays an FM alignment with smaller moments. Therefrom a still sizable net FM moment near $c\sim$0.05 results, whereby the RKKY-like exchange noted in Sec. III B can be held responsible. Intriguingly, close to $c_{\rm p}$ this net FM moment vanishes, accompanied by the disappearance of the Ti-site subclass with FM alignment near OVs. In addition, the nearly exclusive AFM alignment at OVs above $c_{\rm p}$ comes along with zero spin polarization on the remaining Ti sites in the concentration range 0.08<c<0.13. Thus the RKKY-like driven FM phase is followed by a phase region of separated AFM pairs with zero net moment. Though, as discussed before, the *xy orbital* polarization in the 'interstitial' is already active, in this concentration range there is no novel exchange mechanism yet strong enough to *spin* polarize the Ti sites aways from the defects. This changes for $c_{\rm DE}\gtrsim$0.13, when eventually the latter sites build up a considerable xy-dominated magnetic moment. Effective non-local double-exchange between the more-localized $\tilde{e_g}$ electrons near OVs and the more-itinerant xy electrons away from OVs yields net ferromagnetism. Also, part of the AFM alignment of the near-defect Ti sites breaks up and these sites join in the contribution to the FM order. Interestingly, there is a minimum in the averaged $\tilde{e_g}$ magnetic moment on the way to the dense-defect limit. This may be explained by the competition between FM double-exchange and AFM kinetic exchange on Ti near OVs. The increasing electron filling re-strengthens the kinetic exchange close to the defect in the now FM-polarized environment, i.e. a re-formation of AFM pairs occurs. A larger Hund's coupling shifts that minimum to higher electron dopings [see Fig. 8(a)], i.e. the local $\tilde{e_g}$ occupation has to be closer to the kinetic-exchange favored half-filling [cf. Fig. 7(a)] to overcome the $J_{\rm H}$-supported DE processes. We also checked the generic influence of a smaller U=2.5 and encountered an overall somewhat reduced magnetic moment and a weakening of the xy magnetism based on the nonlocal double-exchange.

For the FM phases, our revealed lattice magnetic moment $m_{\rm lat}\sim$0.1-0.2$\mu_{\rm B}$ is in very good agreement with experimental findings [14]. So for moderate $J_{\rm H}$ the nonlocal polarization effect of OVs fosters a sizable xy-dominated magnetic moment on defect-free Ti sites above a concentration $c_{\rm DE}\sim$0.13. This nonlocal double-exchange process extends the local DE mechanism from coherent systems, here active in the dense-defect limit. Note that the obtained magnetic moment $m\sim$0.2$\mu_{\rm B}$ for $J_{\rm H}$=0.55 in the latter limit is in excellent agreement with the former DFT+DMFT results (cf. Fig. 2), highlighting the consistency of the model. However, there is a difference in the orbital contributions, since in the real-space RISB model the $\tilde{e_g}$ level is more strongly spin-polarized than xy. This may be explained by the fact that fluctuations and their correlations, relevant for assessing the DE processes in detail, are underestimated in simplified RISB compared to DMFT with a CT-QMC solver. It could also be that scattering in additional TiO_2 layers, which is not included in the real-space modeling, supports the xy spin polarization.

Finally, we address spectral features at low energy since, e.g., the question arises about the different site and orbital contributions to the resulting metallicity. For selective dopings, Fig. 9 shows the total QP density of states (DOS) as well as the site- and orbital-resolved QP spectral weight within a small energy window around the Fermi level, both in the PM regime. The real-space/orbital resolution is naturally derived from analyzing the low-energy lattice eigenvectors of the renormalized kinetic Hamiltonian.

At the concentration just above $c_{\rm p}$ the total DOS displays a pseudogap-like feature at the Fermi level. From a Stoner argumentation, this reduced spectral weight at ε_F is in line with a vanishing of ferromagnetism in this concentration regime. In the case of higher OV numbers, i.e. higher electron dopings, the low-energy density of states rises again within the DE-FM region. As generally expected the xy weight is mainly located in the defect-free regions, and the $\tilde{e_g}$ weight stems dominantly from defect-near regions. Close to the dilute-defect limit, the overall xy low-energy weight is lower, but it becomes dominant just above $c_{\rm p}$. There the $\tilde{e_g}$ electrons appear most localized, giving eventually rise to the pair-AFM phase. For $c_{\rm DE}\gtrsim$0.13 eventually the $\tilde{e_g}$ low-energy contribution

again overcomes the xy one, marking the intriguing scattering regime of the effective double-exchange region.

IV. SUMMARY AND DISCUSSION

This work examined the key effects of the electronic structure reconstruction in the LAO/STO interface due to the presence of OVs. Different orbital and spin exchange processes are identified for varying OV concentrations. From the revealed and expected magnitudes of hoppings, crystal fields and Coulomb interactions a straightforward picture of fully localized (Kondo-like) electrons near OVs is not evident. Charge self-consistent DFT+DMFT for LAO/STO supercells in a dense-defect limit yields a dichotomy between OV-induced heavier $\tilde{e_g}$ states as well as xy states with a higher QP weight. But itinerancy remains a common feature when including a finite Hund's coupling $J_{\rm H}$. The latter not only triggers the correlation strength but fosters ferromagnetism above a threshold doping through effective nonlocal and local double-exchange processes. Additionally, the strongly correlated dense-defect limit is spectrally marked by a lower Hubbard peak of $\tilde{e_g}$ kind. For generic OV numbers in a 10×10 TiO_2 model interface our correlated real-space RISB approach elucidates further mechanisms due to the system separation into Ti sites near and away from OVs. Coulomb interactions are relevant to trigger intricate (nonlocal) orbital polarization processes, especially at the defect-free Ti sites.

Concerning magnetic order, the schematic phase diagram in Fig. 10 summarizes the main findings. Already in the dilute limit of very few vacancies, oscillations in the sign of the magnetic moments with distance from the OV can be detected. Near OVs two subclasses of Ti sites appear, one favors local AFM and the other local FM alignment. An effective RKKY-like exchange mechanism weakly spin polarizes the system, giving rise to a finite FM net moment. We note that the present RKKY ordering is not conventional in the sense that the involved local moments are comparatively small. Due to the delicate exchange mechanism, the expected Curie temperature T_c associated with this phase is rather low. Above an interface vacancy concentration $c_p{\sim}0.08$, the pairs of AFM-aligned Ti sites dominate the lattice and the spin polarization in the regions without OVs disappears until at $c_{\rm DE}{\sim}0.13$ the double-exchange becomes strong enough to polarize the 'interstitial', now with dominant xy character. In addition, the DE mechanism is effective in switching local AFM pairs to FM alignment. A more robust ferromagnetic order sets in, with a supposedly much larger T_c, and continues to be stable up to the dense-defect limit. The value of $J_{\rm H}$ influences the competition between $\tilde{e_g}$ filling-controlled re-strengthened AFM-like kinetic exchange and the DE processes near OVs in this novel DE-FM phase. We did not delve into the possible phase transitions among the three phases. Because of the overall defect system without a coherent local order parameter and straightforward symmetry distinction, first-order(-like) transitions with coexistence regions are expected (cf. Fig. 10).

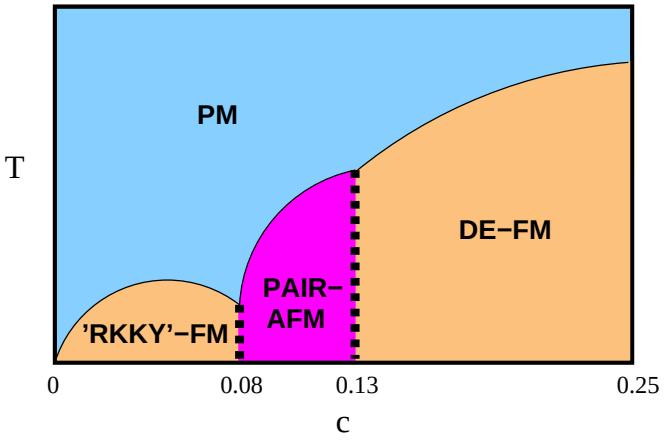

FIG. 10. (color online) Rough sketch of a finite-temperature (T) magnetic phase diagram for OV concentrations c based on the real-space RISB modeling of the LAO/STO interface. Dashed phase boundaries of the pair-AFM phase mark the possible occurrence of coexistence regions with the nearby FM phases.

Our obtained behavior with increasing OV concentration shares several features with experimental results. It is generally in accordance with the found key dependence of magnetism on electron doping in STO-based materials. An interplay of AFM and FM tendencies has been recently identified by Bi *et al.* [28]. The different experimental results concerning the range of stability for LAO/STO ferromagnetism may be related to substantial differences in the number of vacancies in the respective samples. Whereas nearly stoichiometric interfaces are susceptible to the low-T_c RKKY-like FM phase [59, 60], OV-rich samples can stabilize the DE-FM phase with the surprisingly high T_c near room temperature [13, 28]. Of course, such different ferromagnetism may also emerge in very inhomogeneous samples. A theoretical resolution of phase separation on a larger lattice scale based on the present modeling is, however, numerically hard to achieve. Concerning the crucial concentration dependence, unique behavior connected to critical electron densities has been revealed in magnetotransport measurements [23]. In that respect it would be very interesting to trace in detail the ferromagnetism in applied magnetic field B within a group of samples with different OV concentrations, or to perform in-situ monitoring with oxygen pressure. For instance, the pair-AFM phase could be transformed to FM order by a larger field B.

We have shown that itinerancy, polarized orbital degrees of freedom and magnetic order naturally go together in LAO/STO interfaces with OVs. The realistic many-body physics remains challenging and needs further work. From theory, the treatment of the full Ti($3d$) shell for the demanding supercell- and real-space compu-

tations would allow for a more detailed orbital resolution. Including the impact of spin-orbit coupling and the competition of the revealed phases with superconductivity is a natural further modeling step. In addition, with even larger numerical effort by further extension to a cluster-RISB framework [50], one could introduce a two-site cluster in real space for each pair of Ti sites linked by an OV. Then possible singlet formation, contrary to the here-described local pair-AFM state, via intersite self-energies would be describable. Note that we have limited our work to single-OV defects. An investigation of multi-OV configurations up to vacancy-clustered regions on very large real-space lattices will surely be appreciated future work. In this respect, experimental information on defect concentrations, locations, and arrangements beyond currently available data is greatly needed.

Generally, controlling the defect structure within interfaces of oxide heterostructures will be pivotal to eventually engineering technological applications with designated response behavior. Recent findings of room-temperature ferromagnetism and enhanced photocatalytic performance in Ti-defected TiO_2 Anatase [61] are a further example for the relevance and potential of defect-induced oxide physics beyond the high-T_c cuprate paradigm. The here-documented sensitivity of the (magnetic) electronic structure to the OV concentration could be useful not just for designing LAO/STO-based magnetic order at elevated temperatures. Charge and magnetic writing, flexible spintronic switches, sensor technology, and possible multiferroic response are only a few further optional engineering directions. The idea of creating atom-resolved orbital and spin polarization by controlled defect manipulation within a well-defined interface region has so far not been translated into practicable device physics. Defect control of emerging interface phases could be complementary to the technological potential of adatom-driven surface phenomena. The real-space approach presented here is especially suited to simulate and direct such design and control of challenging correlated materials on a nano scale.

ACKNOWLEDGMENTS

We are grateful to T. Kopp, N. Pavlenko and C. Piefke for helpful discussions. This research was supported by the Deutsche Forschungsgemeinschaft through FOR1346 and SFB925. Computations were performed at Regionales Rechenzentrum (RRZ) of the University of Hamburg and at the JUROPA Cluster of the Jülich Supercomputing Centre (JSC) under Project No. hhh08.

[1] A. Kalabukhov, R. Gunnarsson, J. Börjesson, E. Olsson, T. Claeson, and D. Winkler, Phys. Rev. B **75**, 121404(R) (2007).
[2] W. Siemons, G. Koster, H. Yamamoto, W. A. Harrison, G. Lucovsky, T. H. Geballe, D. H. A. Blank, and M. R. Beasley, Phys. Rev. Lett. **98**, 196802 (2007).
[3] M. Salluzzo, S. Gariglio, D. Stornaiuolo, V. Sessi, S. Rusponi, C. Piamonteze, G. M. DeLuca, M. Minola, D. Marré, A. Gadaleta, H. Brune, F. Nolting, N. B. Brookes, and G. Ghiringhelli, Phys. Rev. Lett. **111**, 087204 (2013).
[4] Z. Q. Liu, C. J. Li, W. M. Lü, X. H. Huang, Z. Huang, S. W. Zeng, X. P. Qiu, L. S. Huang, A. Annadi, J. S. Chen, J. M. D. Coey, T. Venkatesan, and Ariando, Physical Review X **3**, 021010 (2013).
[5] A. David, Y. Tian, P. Yang, X. Gao, W. Lin, A. B. S. amd J.-M. Zuo, W. Prellier, and T. Wu, Scientific Reports **5**, 10255 (2015).
[6] A. F. Santander-Syro, O. Copie, T. Kondo, F. Fortuna, S. Pailhè, R. Weht, X. G. Qiu, F. Bertran, A. Nicolaou, A. Taleb-Ibrahimi, P. L. Fèvre, G. Herranz, M. Bibes, N. Reyren, Y. Apertet, P. Lecoeur, A. Barthélémy, and M. J. Rozenberg, Nature **469**, 189 (2011).
[7] W. Meevasana, P. D. C. King, R. H. He, S.-K. Mo, M. Hashimoto, A. Tamai, P. Songsiriritthigul, F. Baumberger, and Z.-X. Shen, Nat. Mat. **10**, 114 (2011).
[8] S. M. Walker, A. de la Torre, F. Y. Bruno, A. Tamai, T. K. Kim, M. Hoesch, M. Shi, M. S. Bahramy, P. C. King, and F. Baumberger, Phys. Rev. Lett. **113**, 177601 (2014).
[9] W. D. Rice, P. Ambwani, M. Bombeck, J. D. Thompson, G. Haugstad, C. Leighton, and S. A. Crooker, Nature Mat. **13**, 481 (2014).
[10] N. Reyren, S. Thiel, A. D. Caviglia, L. F. Kourkoutis, G. Hammerl, C. Richter, C. W. Schneider, T. Kopp, A.-S. Rüetschi, D. Jaccard, M. Gabay, D. A. Muller, J.-M. Triscone, and J. Mannhart, Science **317**, 1196 (2007).
[11] A. Brinkman, M. Huijben, M. van Zalk, J. Huijben, U. Zeitler, J. C. Maan, W. G. van der Wiel, G. Rijnders, D. H. A. Blank, and H. Hilgenkamp, Nature Mater. **6**, 493 (2007).
[12] Y. Li, S. N. Phattalung, S. Limpijumnong, J. Kim, and J. Yu, Phys. Rev. B **84**, 245307 (2011).
[13] Ariando, X. Wang, G. Baskaran, Z. Q. Liu, J. Huijben, J. B. Yi, A. Annadi, A. R. Barman, A. Rusydi, S. Dhar, Y. P. Feng, J. Ding, H. Hilgenkamp, and T. Venkatesan, Nature Commun. **2**, 188 (2011).
[14] J.-S. Lee, Y. W. Xie, H. K. Sato, C. Bell, Y. Hikita, H. Y. Hwang, and C.-C. Kao, Nature Mat. **12**, 703 (2013).
[15] R. Pentcheva and W. E. Pickett, Phys. Rev. B **74**, 035112 (2006).
[16] N. Pavlenko, T. Kopp, E. Y. Tsymbal, G. A. Sawatzky, and J. Mannhart, Phys. Rev. B **85**, 020407(R) (2012).
[17] J. Shen, H. Lee, R. Valentí, and H. O. Jeschke, Phys. Rev. B **86**, 195119 (2012).
[18] C. Lin and A. A. Demkov, Phys. Rev. Lett. **111**, 217601 (2013).
[19] F. Lechermann, L. Boehnke, D. Grieger, and C. Piefke, Phys. Rev. B **90**, 085125 (2014).
[20] M. Breitschaft, V. Tinkl, N. Pavlenko, S. Paetel, C. Richter, J. R. Kirtley, Y. C. Liao, G. Hammerl, V. Eyert, T. Kopp, and J. Mannhart, Phys. Rev. B **81**, 153414

(2010).
[21] Z. Ristic, R. DiCapua, F. Chiarella, G. M. DeLuca, I. Maggio-Aprile, M. Radovic, and M. Salluzzo, Phys. Rev. B **86**, 045127 (2012).
[22] W. Sitaputra, N. Sivadas, M. Skowronski, D. Xiao, and R. M. Feenstra, Phys. Rev. B **91**, 205408 (2015).
[23] A. Joshua, J. Ruhman, S. Pecker, E. Altman, and S. Ilani, PNAS **110**, 9633 (2013).
[24] K.-J. Zhou, M. Radovic, J. Schlappa, V. Strocov, R. Frison, J. Mesot, L. Patthey, and T. Schmitt, Phys. Rev. B **83**, 201402(R) (2011).
[25] J. Park, B.-G. Cho, K. D. Kim, J. Koo, H. Jang, K.-T. Ko, J.-H. Park, K.-B. Lee, J.-Y. Kim, D. R. Lee, C. A. Burns, S. S. A. Seo, and H. N. Lee, Phys. Rev. Lett. **110**, 017401 (2013).
[26] G. Berner, M. Sing, H. Fujiwara, A. Yasui, Y. Saitoh, A. Yamasaki, Y. Nishitani, A. Sekiyama, N. Pavlenko, T. Kopp, C. Richter, J. Mannhart, S. Suga, , and R. Claessen, Phys. Rev. Lett. **110**, 247601 (2013).
[27] J. A. Sulpizio, S. Ilani, P. Irvin, and J. Levy, Annu. Rev. Mater. Res. **44**, 117 (2014).
[28] F. Bi, M. Huang, S. Ryu, H. Lee, C.-W. Bark, C.-B. E. amd P. Irvin, and J. Levy, Nature Commun. **5**, 5019 (2014).
[29] C. W. Bark, P. Sharma, Y. Wang, S. H. Baek, S. Lee, S. Ryu, C. M. Folkman, T. R. Paudel, A. Kumar, S. V. Kalinin, A. Sokolov, E. Y. Tsymbal, M. S. Rzchowski, A. Gruverman, and C. B. Eom, Nano Lett. **12**, 1765 (2012).
[30] I. R. Shein and A. L. Ivanovskii, Phys. Lett. A **371**, 155 (2007).
[31] R. L. Johnson-Wilke, D. Marincel, S. Zhu, M. P. Warusawithana, A. Hatt, J. Sayre, K. T. Delaney, R. Engel-Herbert, C. M. Schlepütz, J.-W. Kim, V. Gopalan, N. A. Spaldin, D. G. Schlom, P. J. Ryan, and S. Trolier-McKinstry, Phys. Rev. B **88**, 174101 (2013).
[32] J. C. Li, J. I. Beltrán, and M. C. Muñoz, Phys. Rev. B **87**, 075411 (2013).
[33] A. Janotti, J. B. Varley, M. Choi, and C. G. Van de Walle, Phys. Rev. B **90**, 085202 (2014).
[34] A. Lopez-Bezanilla, P. Ganesh, and P. B. Littlewood, Phys. Rev. B **92**, 115112 (2015).
[35] D. Grieger and F. Lechermann, Phys. Rev. B **90**, 115115 (2014).
[36] K. Michaeli, A. C. Potter, and P. A. Lee, Phys. Rev. Lett. **108**, 117003 (2012).
[37] G. Chen and L. Balents, Phys. Rev. Lett. **110**, 206401 (2013).
[38] S. Banerjee, O. Erten, and M. Randeria, Nature Phys. **9**, 626 (2013).
[39] J. Ruhman, A. Joshua, S. Ilani, and E. Altman, Phys. Rev. B **90**, 125123 (2013).
[40] L. Yu and A. Zunger, Nat. Commun. **5**, 5118 (2014).
[41] C. Lin and A. A. Demkov, Phys. Rev. Lett. **113**, 157602 (2014).
[42] N. Pavlenko, T. Kopp, and J. Mannhart, Phys. Rev. B **88**, 201104(R) (2013).
[43] C. Zener, Phys. Rev. **82**, 403 (1951).
[44] P. W. Anderson and H. Hasegawa, Phys. Rev. **100**, 675 (1955).
[45] H. Y. Hwang, Y. Iwasa, M. Kawasaki, B. Keimer, N. Nagaosa, and Y. Tokura, Nature Materials **11**, 103 (2012).
[46] A. N. Rubtsov, V. V. Savkin, and A. I. Lichtenstein, Phys. Rev. B **72**, 035122 (2005).
[47] P. Werner, A. Comanac, L. de' Medici, M. Troyer, and A. J. Millis, Phys. Rev. Lett. **97**, 076405 (2006).
[48] O. Parcollet, M. Ferrero, T. Ayral, H. Hafermann, I. Krivenko, L. Messio, and P. Seth, Computer Physics Communications **196**, 398 (2015).
[49] L. Boehnke, H. Hafermann, M. Ferrero, F. Lechermann, and O. Parcollet, Phys. Rev. B **84**, 075145 (2011).
[50] F. Lechermann, A. Georges, G. Kotliar, and O. Parcollet, Phys. Rev. B **76**, 155102 (2007).
[51] B. Amadon, F. Lechermann, A. Georges, F. Jollet, T. O. Wehling, and A. I. Lichtenstein, Phys. Rev. B **77**, 205112 (2008).
[52] T. Li, P. Wölfle, and P. J. Hirschfeld, Phys. Rev. B **40**, 6817 (1989).
[53] J. Bünemann, W. Weber, and F. Gebhard, Phys. Rev. B **57**, 6896 (1998).
[54] F. Lechermann, Phys. Rev. Lett. **102**, 046403 (2009).
[55] L. Huang, L. Du, and X. Dai, Phys. Rev. B **86**, 035150 (2012).
[56] E. C. Andrade, E. Miranda, and V. Dobrosavljević, Phys. Rev. Lett. **102**, 206403 (2009).
[57] G. Kotliar and A. E. Ruckenstein, Phys. Rev. Lett. **57**, 1362 (1986).
[58] F. Lechermann, S. Biermann, and A. Georges, Prog. Theor. Phys. Suppl. **160**, 233 (2005).
[59] M. R. Fitzsimmons, N. W. Hengartner, S. Singh, M. Zhernenkov, F. Y. Bruno, J. Santamaria, A. Brinkman, M. Huijben, H. J. A. Molegraaf, J. de la Venta, , and I. K. Schuller, Phys. Rev. Lett. **107**, 217201 (2011).
[60] A. Ron, E. Maniv, D. Graf, J.-H. Park, and Y. Dagan, Phys. Rev. Lett. **113**, 216801 (2014).
[61] S. Wang, L. Pan, J.-J. Song, W. Mi, J.-J. Zou, L. Wang, and X. Zhang, J. Am. Chem. Soc. (2015).